

# The Mean Ultraviolet Spectrum of a Representative Sample of Faint $z \sim 3$ Lyman Alpha Emitters

Kimihiko Nakajima,<sup>1</sup>★ Thomas Fletcher,<sup>2</sup> Richard S. Ellis,<sup>1,2</sup> Brant E. Robertson,<sup>3</sup> and Ikuru Iwata<sup>4</sup>

<sup>1</sup>*European Southern Observatory, Karl-Schwarzschild-Str. 2, D-85748, Garching bei München, Germany*

<sup>2</sup>*Department of Physics and Astronomy, University College London, Gower Street, London WC1E 6BT, UK*

<sup>3</sup>*Department of Astronomy and Astrophysics, University of California, Santa Cruz, 1156 High Street, Santa Cruz, CA 95064, USA*

<sup>4</sup>*Subaru Telescope, National Astronomical Observatory of Japan, 650 North Aôhōhoku Place, Hilo, HI 96720, USA*

Accepted for publication in MNRAS on Mar 17, 2018

## ABSTRACT

We discuss the rest-frame ultraviolet emission line spectra of a large ( $\sim 100$ ) sample of low luminosity redshift  $z \sim 3.1$  Lyman alpha emitters (LAEs) drawn from a Subaru imaging survey in the SSA22 survey field. Our earlier work based on smaller samples indicated that such sources have high  $[\text{O III}]/[\text{O II}]$  line ratios possibly arising from a hard ionising spectrum that may be typical of similar sources in the reionisation era. With optical spectra secured from VLT/VIMOS, we re-examine the nature of the ionising radiation in a larger sample using the strength of the high ionisation diagnostic emission lines of  $\text{C III}] \lambda 1909$ ,  $\text{C IV} \lambda 1549$ ,  $\text{He II} \lambda 1640$ , and  $\text{O III}] \lambda \lambda 1661, 1666$  Å in various stacked subsets. Our analysis confirms earlier suggestions of a correlation between the strength of  $\text{Ly}\alpha$  and  $\text{C III}]$  emission and we find similar trends with broad band UV luminosity and rest-frame UV colour. Using various diagnostic line ratios and our stellar photoionisation models, we determine both the gas phase metallicity and hardness of the ionisation spectrum characterised by  $\xi_{\text{ion}}$  - the number of Lyman continuum photons per UV luminosity. We confirm our earlier suggestion that  $\xi_{\text{ion}}$  is significantly larger for LAEs than for continuum-selected Lyman break galaxies, particularly for those LAEs with the faintest UV luminosities. We briefly discuss the implications for cosmic reionisation if the metal-poor intensely star-forming systems studied here are representative examples of those at much higher redshift.

**Key words:** Galaxies: evolution - galaxies: high-redshift

## 1 INTRODUCTION

A continuing debate in the high redshift community is whether early star-forming galaxies generate sufficient photons to govern the reionisation process. The key questions relate to both the nature of the ionising spectrum for low metallicity intensely-star forming systems thought to dominate the redshift interval  $6 < z < 10$ , and the extent to which the circumgalactic medium is transparent to Lyman continuum (LyC) radiation. Detailed diagnostics of these questions are currently challenging to observe for  $z > 6$  sources. The nature of the ionising spectrum, particularly the efficiency of the ionising photon production from the stellar population defined by  $\xi_{\text{ion}}$ , the number of LyC photons per

UV luminosity (e.g., Robertson et al. 2013), is ideally constrained by measures of Balmer emission (Bouwens et al. 2016) interpreted through recombination physics. However, the Balmer emission lines are currently beyond reach of ground-based telescopes at high redshifts. Furthermore, due to the rapid increase in intergalactic absorbers LyC leakage from galaxies at  $z > 6$  cannot be directly measured (e.g. Madau 1995; Inoue & Iwata 2008; Inoue et al. 2014). For these reasons, attention has focused on identifying and studying possible analogues of low metallicity galaxies at low (e.g., Leitherer et al. 2016; Izotov et al. 2016a,b; Schaerer et al. 2016; Verhamme et al. 2017) and intermediate redshifts (e.g., Iwata et al. 2009; Nestor et al. 2013; Vanzella et al. 2016a,b; Amorín et al. 2017).

Low metallicity, low mass systems such as narrow-band selected Lyman alpha emitters (LAEs) at intermediate red-

★ JSPS Overseas Research Fellow; E-mail: knakajim@eso.org

**Table 1.** Summary of Optical Imaging Data.

Band	Field	Observatory	PSF	$m_{\text{lim}}$	Reference
			(1)	(2)	(3)
<i>NB497</i>	SSA22	Subaru	1.0	26.2	(a), (b), (c)
<i>B</i>	SSA22	Subaru	1.0	26.5	(a), (b), (c)
<i>V</i>	SSA22	Subaru	1.0	26.6	(a), (b), (c)
<i>R</i>	SSA22	Subaru	1.1	26.7	(a), (c)
<i>i'</i>	SSA22	Subaru	1.0	26.4	(a)
<i>z'</i>	SSA22	Subaru	1.0	25.7	(a)

(1) FWHM in arcsec. (2)  $5\sigma$  limiting magnitude estimated by  $2''$  diameter aperture photometry. (3) (a) Hayashino et al. (2004); (b) Yamada et al. (2012); (c) Matsuda et al. (2004).

shift may provide valuable examples of sources contributing to cosmic reionisation. In a recent paper (Nakajima et al. 2016) we have demonstrated for a modest sample of 15  $z \sim 3$  LAEs that  $[\text{O III}]\lambda\lambda 5007, 4959$  emission is unusually intense compared to  $[\text{O II}]\lambda 3727$ , contrary to similar measurements of the more metal rich Lyman break population (LBGs). We showed that this enhanced  $[\text{O III}]$  is unlikely to be the result of a lower metallicity alone and may arise, at least partially, from a harder ionising spectrum. Since intense  $[\text{O III}]$  emission appears to be a common feature of sources in the reionisation era, as inferred from *Spitzer*/IRAC broad band photometry (Schenker et al. 2013; Smit et al. 2014, 2015; Roberts-Borsani et al. 2016), we argued that intrinsically faint  $z \sim 3$  LAEs may be valuable analogues of the dominant population of faint sources which may govern reionisation. Their importance in understanding the early universe also arises from the fact that the relative fraction of all star-forming galaxies showing strong Lyman alpha emission increases with redshift up to the reionisation era (e.g., Stark et al. 2011; Curtis-Lake et al. 2012; Cassata et al. 2015).

In this paper we attempt to further constrain the nature of the ionising radiation, i.e., the efficiency of the LyC photon production characterised by  $\xi_{\text{ion}}$ , for a much larger sample of  $\sim 100$   $z \sim 3$  LAEs drawn from the same parent dataset as in Nakajima et al. (2016) via constraints on the strength of high ionisation UV metal lines, principally  $\text{C III}]\lambda 1909$  and  $\text{C IV}]\lambda 1549$  which are redshifted into the optical at  $z \approx 3.1$ <sup>1</sup>. This approach follows a similar analysis undertaken for sub-luminous lensed Lyman break galaxies at  $z \sim 2-3$  (Stark et al. 2014) interpreted with photoionisation codes (e.g., Nakajima & Ouchi 2014; Feltre et al. 2016; Gutkin et al. 2016; Nakajima et al. 2017) which also supported the notion of a harder ionising radiation field compared to local sources.

A plan of the paper follows. In §2 we introduce the sample targeted for follow-up spectroscopy which is drawn from a field previously surveyed with narrow-band filters with the Subaru telescope. We discuss the observations undertaken with both the Keck and ESO VLT telescopes and the tech-

<sup>1</sup> The  $\text{C III}]\lambda 1909$ , or simply  $\text{C III}]$ , refers to the sum of the  $[\text{C III}]\lambda 1907$  and  $[\text{C III}]\lambda 1909$ . The  $\text{C IV}]\lambda 1549$ , or  $\text{C IV}]$ , quotes the  $\text{C IV}$  doublet of  $\lambda = 1548 \text{ \AA}$  and  $1550 \text{ \AA}$ .

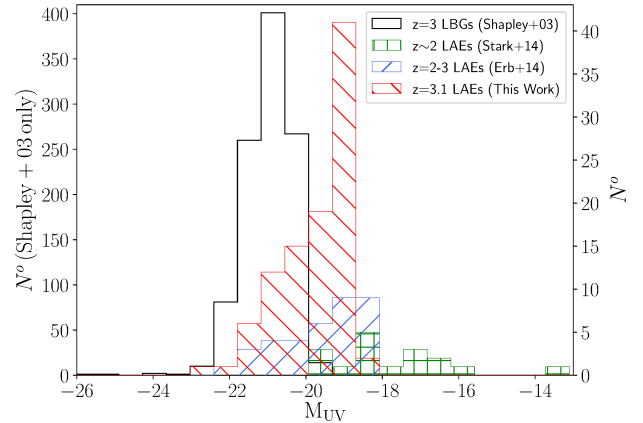


**Figure 1.** UV absolute magnitude distributions for recently-published rest-frame UV spectroscopic studies at  $z = 2 - 4$ . Our VIMOS sample is plotted with the red hatched histogram. Other datasets include Lyman break galaxies: Shapley et al. (2003) in black (numbers in the left ordinate) and Erb et al. (2014) in blue, and gravitationally-lensed galaxies from Stark et al. (2014) in green.

niques used to reduce these data. In §3 we discuss the spectroscopic results in terms of the success rates of recovering Ly $\alpha$  emission in the two observational campaigns and the velocity offset of Ly $\alpha$ ,  $\Delta v_{\text{Ly}\alpha}$ , relative to the systemic velocity inferred from nebular lines. The relationship between  $\Delta v_{\text{Ly}\alpha}$  and the equivalent width ( $\text{EW}(\text{Ly}\alpha)$ ) is then used to stack the higher quality ESO spectra in various ways. Furthermore, we interpret these spectroscopic stacks and provide constraints on the ratios of various UV metal lines which we interpret with photoionisation models thereby deriving measures of the gas phase metallicity and hardness of the ionising spectrum. We discuss the implications of our results and present a summary in §4.

We assume a  $\Lambda$ CDM cosmology using the Planck results with  $\Omega_M=0.308$ ,  $\Omega_\Lambda=0.692$  and  $H_0=67.8 \text{ km s}^{-1} \text{ Mpc}^{-1}$ . We adopt a solar chemical composition following Asplund et al. (2009).

## 2 SPECTROSCOPIC DATA

### 2.1 Sample

Our target sample of  $z \sim 3.1$  Lyman alpha emitters (LAEs) is drawn from earlier panoramic narrow-band imaging surveys undertaken with the Subaru Telescope. In our previous paper (Nakajima et al. 2016, hereafter Paper I), we secured near-infrared spectra sampling  $[\text{O II}]$ ,  $\text{H}\beta$  and  $[\text{O III}]$  emission for 15 sources in the SSA22 field (Hayashino et al. 2004; Yamada et al. 2012; Micheva et al. 2017) using Keck/MOSFIRE. 13 of these 15 objects are LAEs with  $\text{EW}(\text{Ly}\alpha) > 20 \text{ \AA}$  and the remaining two are Lyman break galaxies (LBGs) also at  $z \approx 3.1$ . The present enlarged sample is drawn from 281 LAEs in the same field (SSA22-Sb1; Yamada et al. 2012) including the 13 MOSFIRE-identified LAEs selected via their photometric excess in a narrowband filter centred at 497 nm. In order to obtain rest-frame UV spectra to further our studies of the

**Table 2.** Summary of the VIMOS observation for the  $z = 3.1$  LAEs.

Instrument	Field	Date of obs.	Exposure times (hrs)	Wavelength coverage (Å)	$R$	$N^o$ of LAEs [LBGs] <sup>(†)</sup>	
						Observed	Identified
VIMOS	SSA22	2016 Aug & Oct	11.0 (quads. #1–3)	4850 – 9450	580	72 [10]	59 [1] <sup>(‡)</sup>
			7.0 (quad. #4)			12 [3]	6 [1]

(†) Numbers of LBGs are given in the square brackets. (‡) Three additional LBGs that lack Ly $\alpha$  emission are identified with UV absorption lines.

nature of this population, we conducted deep optical spectroscopy of a subset of these photometrically-identified LAEs using the VLT/VIMOS spectrograph. Optical spectroscopy was also obtained using the Keck/LRIS spectrograph in a second SXDS field for which MOSFIRE data is available (Fletcher et al 2018, in prep). That data is only used here to enlarge the sample for which Ly $\alpha$  velocity offsets can be determined (§3.1).

In the VIMOS sample we secured UV spectra for 7 of the 13 LAEs and one of the two LBGs in the SSA22 field for which MOSFIRE spectra are available from Paper I. Additionally, we sampled a further 77 LAEs and 12 LBGs. In total, our new enlarged sample of rest-frame optical spectroscopy comprises 84 LAEs and 13 LBGs, representing a considerable advance over the sample discussed in Paper I. Finally, we have likewise recently enlarged the sample for which MOSFIRE near-infrared spectra is available (Nakajima et al 2018, in prep). This data provides new rest-frame optical emission lines for 6 LAEs and 2 LBGs and is also only used here to improve our understanding of the Ly $\alpha$  velocity offsets (§3.1). Further details of the observations are given in the following subsection.

An important advantage of selecting the SSA22 field is the plentiful deep multi-wavelength photometric data. The optical broadband data is useful in constraining the nature of the stellar populations, such as the absolute UV magnitude  $M_{UV}$  and the UV continuum slope parameter  $\beta$ . We derive the absolute UV magnitude using  $R$ -band photometry which traces the rest frame spectral energy distribution (SED) around 1500–1600 Å, and the UV continuum slope  $\beta$  is measured assuming a power-law fit to the  $R$ ,  $i$ , and  $z$ -band photometry according to the convention  $f_\lambda \propto \lambda^\beta$ . Such  $\beta$  measurements are thus only possible for those LAEs detected in at least two of the Subaru  $R$ ,  $i$ , and  $z$ -band images. A resulting distribution of the UV slope is  $\beta \approx -1.6 \pm 0.8$ , which corresponds to  $E(B - V) \approx 0.09 \pm 0.07$  with the SMC extinction curve and the BPASS SEDs (Reddy et al. 2018). This is comparable to the results of other photometric studies of LAEs at similar redshifts, where  $\beta$  values are calculated as in Meurer et al. (1997) (e.g., Nilsson et al. 2009) and  $E(B - V)$  via SED fitting analysis (e.g., Ono et al. 2010; Nilsson et al. 2011; Guaita et al. 2011; Kusakabe et al. 2018). Finally, although the VIMOS spectra are crucial in confirming the Ly $\alpha$  emission, they cannot provide accurate measures of the equivalent width (EW) of Ly $\alpha$  due to the low signal-to-noise of the UV continuum and aperture effects inevitable with slit spectroscopy (e.g., Momose et al. 2016; Wisotzki et al. 2016). It is preferable, therefore, to measure EWs of Ly $\alpha$  from the BV – NB497 colours, where BV stands for a combination of the B and V broad-band images as (2B+V)/3

(Hayashino et al. 2004). This can be done by using the Ly $\alpha$  observed wavelength in the EW calculation and taking into account the narrow-band and broad-band filter transmission curves to accurately translate the BV – NB497 colour into the EW. The limiting depths of the relevant broad-band photometry in the SSA22 field are given in Table 1.

It is useful to compare the properties of our new spectroscopic sample with those for which similar line emission studies have been undertaken. Fig. 1 compares the UV luminosity distribution of our 97 targets with those for other  $z \approx 2$ – $3$  star-forming galaxies (Shapley et al. 2003; Erb et al. 2014; Stark et al. 2014). Our LAE sample probes a  $M_{UV}$  range from  $-22.4$  down to  $-18.7$  with a median value of  $-19.5$ . Notably, 15 of our LAEs are fainter than the broad-band detection limit ( $M_{UV} \gtrsim -18.7$ ) and the 800 or so UV-selected LBGs from Shapley et al. (2003) with  $R \sim 24.4$  –  $24.9$ , corresponding to  $M_{UV}$  of  $-21.1$  to  $-20.6$ . Only the 16 gravitationally-lensed galaxies at  $z = 1.6$  –  $3$  studied by Stark et al. (2014) overlaps our luminosity range. That sample extends from  $M_{UV} = -19.9$  down to  $-13.7$ .

## 2.2 VIMOS Observations

The VIMOS spectroscopic observations were undertaken in the SSA22 field on UT3 of the VLT in Service Mode (ID: 098.A-0010(A), PI; Ellis) in August – October 2016. A single VIMOS pointing was adopted, comprising a slit mask across four quadrants of the instrument with a field of view of  $4 \times 7' \times 8'$ . To mitigate atmospheric dispersion, the slit-let position angle is restricted to PA =  $90^\circ$  and the field centre was chosen to maximise the number of targets for which [O III] $\lambda 5007$  had been detected already with MOSFIRE (Paper I). Seven LAEs and one LBG from Paper I fell in one quadrant (# 3) and the remaining sample totalling 97 sources included 77 new LAEs at  $z = 3.1$  and 12 LBGs at  $z = 3$ – $4$  as well as the 8 MOSFIRE objects. The new sample of 77 LAEs was drawn uniformly from the parent catalogue and has a median  $M_{UV}$  of  $-19.5$ .

We observed in medium-resolution mode with the GG475 order sorting filter which provided a wavelength coverage from  $\sim 4800$  Å to  $\sim 1 \mu\text{m}$  at a mean spectral resolution of  $R \sim 580$  with a slit width of  $1''$ . Our observation comprised 13 identical observing blocks (OBs), each with an on-source integration of  $3 \times 20$  min using a three point offset pattern along the slit. Relatively bright stars were included on each quadrant adopted to monitor sky conditions and mask alignment. Two of the 13 OBs were discarded as the seeing inferred was  $\gtrsim 1''$ . For quadrant #4, the first 5 OBs, one of which was under a poor seeing condition, were lost due to either an improper alignment or mis-insertion of the

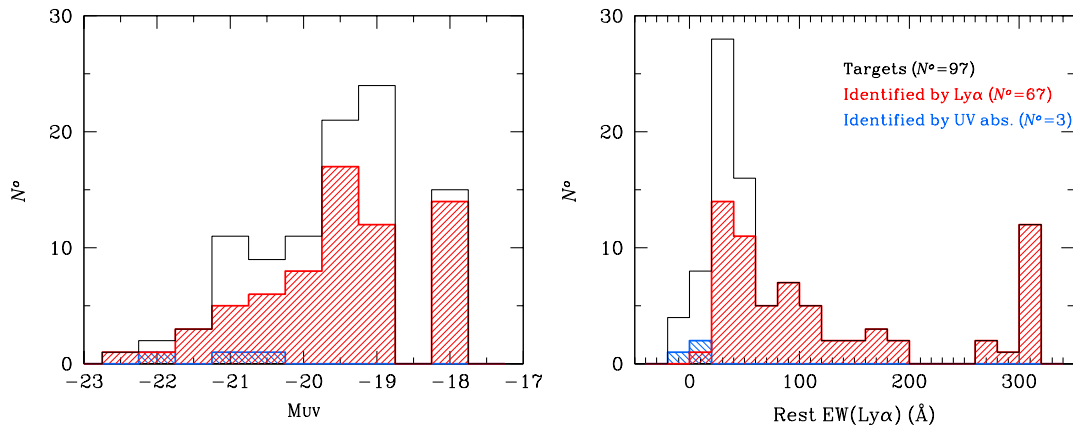


**Figure 2.** Distributions of  $M_{UV}$  (left) and  $EW(Ly\alpha)$  (right) for the VIMOS sample. Red hatched histograms show the numbers of galaxies whose  $Ly\alpha$  is spectroscopically confirmed, and the blue histogram presents LBGs identified via UV absorption line(s). LAEs whose UV continuum was not detected in the Subaru images are assigned to  $M_{UV} > -18.5$  and  $EW(Ly\alpha) > 300 \text{ \AA}$ .

milled mask. The other three quadrants in these 5 OBs were unaffected, since mask alignment was performed excluding the alignment stars in quadrant #4. We thus discarded 4 additional OBs' data for quadrant #4.

In summary, therefore, we obtained in total 11 hrs of on-source integration data for objects in the quadrants #1, 2, and 3, and 7 hrs in the quadrant #4. The typical seeing for the acceptable OBs was  $0''.75$ .

The VIMOS data was reduced using recipes in the standard ESO VIMOS pipeline (v.3.1.7) operated through esoreflex (v.2.8.5). For each OB, the process included bad pixel cleaning, bias subtraction, flat-field correction, frame combination, sky fringing correction, wavelength calibration, and flux calibration. We performed wavelength calibration and flat field using relevant frames taken after each OB. Using the slit position of each science target output by the VIMOS pipeline, we extracted the individual 2D spectrum. Sky subtraction was performed with a low-order polynomial fit along the slit for each wavelength. The 2D spectra were corrected for Galactic extinction based on the  $E(B-V)$  map of Schlegel et al. (1998). Finally, we combined the individual sky-subtracted 2D spectra ( $N = 11$  for objects in the quadrants #1, 2, and 3, and  $N = 7$  in the quadrant #4) with a sigma-clipped average to produce a final 2D spectrum for each of the science targets. 1D spectra were produced for those targets for which at least one emission line could be identified (normally  $Ly\alpha$ ) adding up 9 pixels along the spatial direction centred on the detected emission line. This width was chosen to maximise the signal-to-noise ratio and corresponds approximately to twice the seeing size.

### 2.3 Spectroscopic Confirmations

Our initial task is to spectroscopically confirm the validity of the photometric identifications of  $Ly\alpha$  emission at the expected redshift of  $z \approx 3.1$ . Earlier work drawn from the same Subaru narrow-band imaging survey (Hayashino et al. 2004) has found a typical success rate of  $\approx 66\%$  (Matsuda et al. 2005) (see §3.1). Initially therefore, two authors independently examined the VIMOS spectra for detectable  $Ly\alpha$

emission through visual inspection of both the 1-D and 2-D spectra separately. Such an approach was considered adequate given that the wavelength of  $Ly\alpha$  emission is accurately predicted by the narrowband filters.

Applying a  $3\sigma$  signal to noise limit for the line detections, this investigation resulted in a confirmed list of 65  $z = 3.1$  LAEs corresponding to a relative success rate is  $77\%$  ( $= 65/84$ ). Figure 2 shows the success rate as a function of  $M_{UV}$  and  $EW(Ly\alpha)$ . Notably, we recover  $Ly\alpha$  emission spectroscopically for 100 % of those LAEs with  $EW(Ly\alpha) > 60 \text{ \AA}$ . The success rate is higher than reported by Matsuda et al. (2005) (66%). We consider this reasonable because (i) our VIMOS observations are deeper than earlier studies, and (ii) our sample probes fainter sources. Among the 16 objects studied with MOSFIRE, both in Paper I and with our most recent campaign (Nakajima et al. 2018, in prep.), 12 show  $Ly\alpha$  emission in the VIMOS spectrum.

From our VIMOS observations we also find 2 out of 13 LBGs show prominent  $Ly\alpha$  emission with rest-frame  $EW$  of  $> 20 \text{ \AA}$ . Hereafter we will refer to these 2 LBGs and the 65 genuine LAEs observed as the “VIMOS-LAEs”. We are confident that such sources cannot be explained as lower- $z$  emitters, such as  $[O\text{ II}]\lambda 3727$  emitters at  $z \approx 0.3$  and  $H\beta$ - or  $[O\text{ III}]\lambda 5007$  emitters at  $z \lesssim 0.03$  because of the lack of stronger emission lines of  $[O\text{ III}]\lambda 5007$  and  $H\alpha$  at the corresponding wavelengths.

At this stage, prior to stacking the VIMOS spectra (§3.2), we also inspected the individual spectra searching for other emission lines. Among the 67 VIMOS-LAEs, only 15 sources reveal additional UV metal lines including:  $C\text{ III}]\lambda 1909$ ,  $O\text{ III}]\lambda 1665$ ,  $He\text{ II}]\lambda 1640$ , and/or  $C\text{ IV}]\lambda 1549 \text{ \AA}$ . Most of these sources (10/15) only present  $C\text{ III}]\lambda 1909$  emission with a tentative detection of the other UV line(s). These sources are generally the brighter subset in the spectroscopic sample, including one galaxy initially selected as a LBG and one LAE known as a Type II AGN (Paper I). We additionally find 3 LBGs whose  $Ly\alpha$  emission is not visible but for which UV absorption lines are detected.

We can now summarise the fruits of our spectroscopic campaign for a total of 97 targets (see Table 2). The cata-



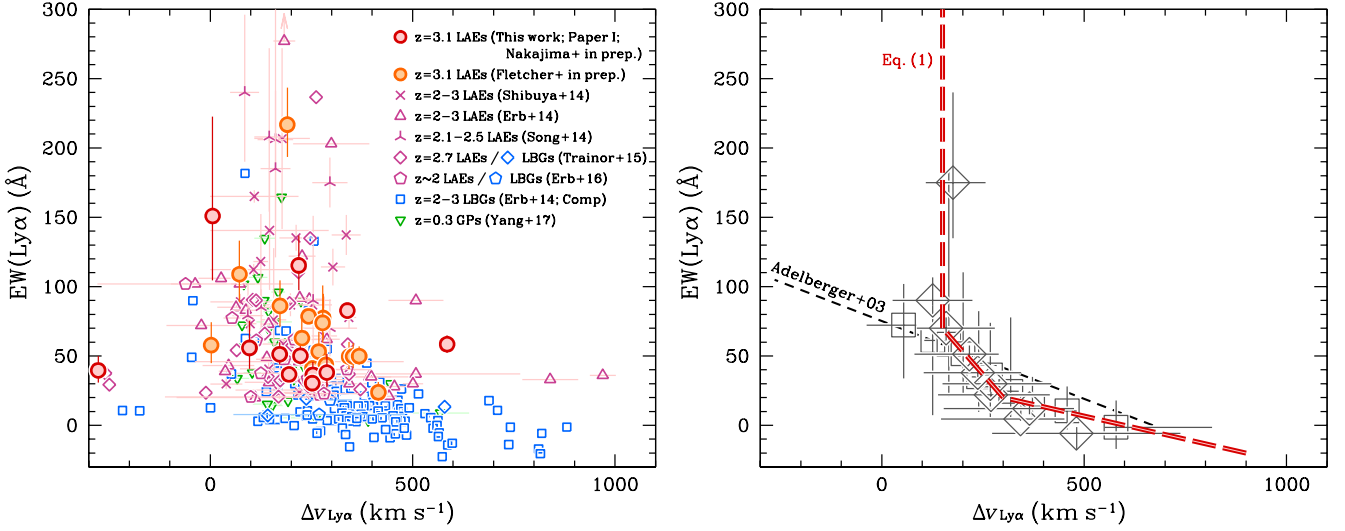


**Figure 3.** (Left:) Relationship between  $EW(Ly\alpha)$  and the velocity offset  $\Delta v_{Ly\alpha}$  for the VIMOS and other samples. Red filled circles represent the newly observed LAEs with VIMOS whose systemic redshift is determined using MOSFIRE detections of [O III] (Paper I). Orange circles show those additional LAEs observed with LRIS and recent MOSFIRE data (see text for details). Magenta, blue and green symbols represent equivalent measures for high redshift LAEs, LBGs with weak  $Ly\alpha$  ( $EW < 20$  Å), and low- $z$  green pea galaxies, respectively (see legend). (Right:) Open grey squares present the average  $EW(Ly\alpha)$  for a  $\Delta v_{Ly\alpha}$  bin, and open grey diamonds show the average  $\Delta v_{Ly\alpha}$  for a  $EW(Ly\alpha)$  bin, using all the individual data points shown in the left panel. The red long-dashed lines is the derived relationship based on Eq. (1), while the black dashed line shows that from Adelberger et al. (2003).

logue summarising which sources have individual metal line detections is provided in Table 5.

### 3 RESULTS

#### 3.1 Ly $\alpha$ emission and its velocity offset

The overlap of 12 confirmed LAEs with our earlier MOSFIRE data (Paper I plus Nakajima et al. 2018, in prep.) and our new  $Ly\alpha$  detections from both VIMOS and LRIS (Fletcher et al 2018, in prep) enables us to revisit the question of the velocity offset of  $Ly\alpha$ ,  $\Delta v_{Ly\alpha}$ , with respect to other nebular lines. This offset is crucial to understand prior to stacking spectra in order to achieve reliable detection of weaker UV metal lines. Traditionally this quantity has been investigated as a function of the EW of  $Ly\alpha$  (Adelberger et al. 2003) and we examine this relationship anew combining both literature data (Shibuya et al. 2014; Erb et al. 2014; Song et al. 2014; Trainor et al. 2015; Erb et al. 2016; Yang et al. 2017) and our own SSA22 measures in Figure 3. As discussed in §2.1 and above, we bring into play both the LRIS and recent MOSFIRE data only for the purpose of increasing the sample size.

Examination of this data suggests a new relationship given by:

$$\begin{aligned} \Delta v_{Ly\alpha} \text{ (km s}^{-1}\text{)} &\approx 150 & (EW > 70 \text{ Å}) \\ &\approx 360 - 3 EW & (EW = 20 - 70 \text{ Å}) \\ &\approx 600 - 15 EW & (EW < 20 \text{ Å}). \end{aligned} \quad (1)$$

Such an anti-correlation between  $EW(Ly\alpha)$  and  $\Delta v_{Ly\alpha}$  has been previously reported in datasets with a wide dynamic range in  $EW(Ly\alpha)$  (e.g., Hashimoto et al. 2013; Shibuya et al. 2014; Erb et al. 2014; Trainor et al. 2015). As

discussed by earlier kinematic studies of LAEs, the column density of H I gas must play a key role in shaping the anti-correlation, with a larger offset from systems of a higher column density. By combining all the individual data points from the literature, we confirm that the correlation becomes steeper toward a smaller  $\Delta v_{Ly\alpha}$ , i.e., that the spread in EW distribution increases with a smaller  $Ly\alpha$  velocity offset. This trend is as theoretically expected (e.g., Zheng & Wallace 2014), as the secondary effects of anisotropy of the system and viewing angle become less significant in a higher column density. We cannot however fully examine the relationship for LAEs with  $EW(Ly\alpha) \gtrsim 100$  Å due to the modest sample size, and thus present an average velocity offset of  $\Delta v_{Ly\alpha} \approx 150 \text{ km s}^{-1}$  for such strong LAEs. The kinematics properties of our LAEs will be discussed in more detail elsewhere. The relation of Eq. (1) appears to be more appropriate than that presented by Adelberger et al. (2003), especially for galaxies showing strong  $Ly\alpha$  emission. We investigate the difference between both relationships in our stacking analysis below.

#### 3.2 Stacked Spectra

Despite our significant integration time, we only directly detect other UV emission lines in a small subset of our data (§2.3, Table 5). To determine the average strengths of CIII] and other diagnostic UV metal lines we adopted the following stacking procedure.

Firstly, we removed the single known AGN (§2.3) from the sample leaving 66 VIMOS-LAEs. Additionally, since their rest-frame optical lines are identified, we included those 4 targets confirmed with MOSFIRE for which  $Ly\alpha$  is not

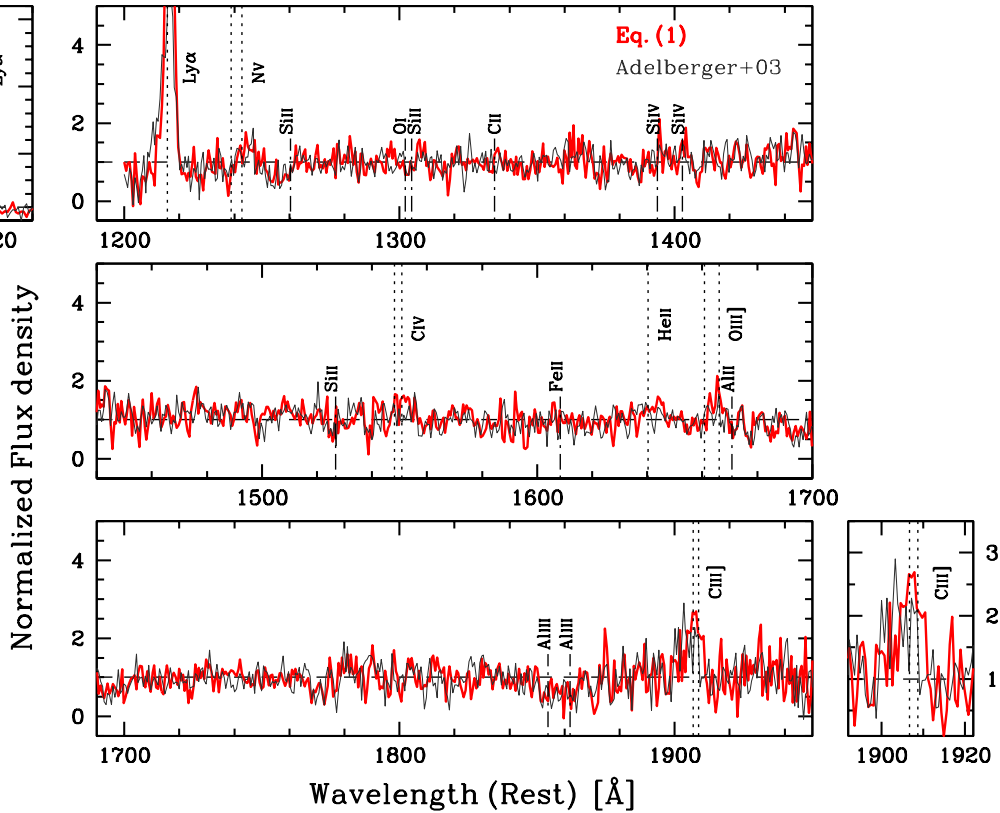


**Figure 4.** The normalised composite rest-frame spectrum for the sample of 70 spectroscopically-confirmed VIMOS LAEs. The thick red spectrum adopts the relationship between  $\Delta v_{\text{Ly}\alpha}$  and  $\text{EW}(\text{Ly}\alpha)$  that we derive with the latest compilation of LAEs and LBGs (i.e., Eq. (1)), while the thin black is based on the [Adelberger et al. \(2003\)](#) relation. Additional panels focus on the  $\text{Ly}\alpha$  and  $\text{C III]}$  emission regions and highlight the difference between the two methods. Wavelengths of additional emission lines and absorption lines are marked with a dotted and dot-dashed vertical line, respectively.

visible in the VIMOS spectrum. The sample available for stacking analyses thus consists of 70 sources.

Using the individual flux-calibrated spectra, we shifted each to the rest-frame as described below, rebinned each to a common dispersion of  $0.65 \text{ \AA}$  per pixel, and scaled to a common median in the wavelength range of  $\sim 1250 - 1500 \text{ \AA}$ . Finally, the spectra were averaged. To exclude positive and negative sky subtraction residuals and cosmic-ray residuals, we rejected an equal number of the highest and lowest outliers at each wavelength corresponding in total to  $\sim 5\%$  of the data. We confirmed that median-stacked composite spectra generated in the same way were almost indistinguishable from the average-stacked ones.

To define a systemic redshift for each galaxy, we adopted a similar approach used by [Shapley et al. \(2003\)](#). We used the rest-frame optical redshifts for the MOSFIRE identified objects in SSA22 (Paper I; Nakajima et al. in prep.). For the others, we estimated a systemic redshift from the  $\text{Ly}\alpha$  using the updated formula given by Eq. (1).

The normalised composite spectrum for the entire sample is shown in red in Figure 4; that adopted using [Adelberger et al. \(2003\)](#)’s velocity offset prescription is shown in black. The most striking difference is found around the  $\text{Ly}\alpha$  emission. The red spectrum presents a prominent, asymmetric line. On the other hand, the black shows a less peaked signal with a broad tail to the blue side of the emission. This originates from the simple linear relation of

[Adelberger et al. \(2003\)](#),  $\Delta v_{\text{Ly}\alpha} \approx 670 - 8.9\text{EW}$ , whereby a fraction of the VIMOS LAEs with  $\text{EW} \gtrsim 75 \text{ \AA}$  would be predicted to have a blueshifted  $\text{Ly}\alpha$  emission with respect to the systemic redshift. We can also evaluate the validity of the composite method by measuring the EWs of  $\text{Ly}\alpha$ . We determine the  $\text{EW}(\text{Ly}\alpha)$  from the black and red spectrum as  $31 \pm 8 \text{ \AA}$  and  $67 \pm 17 \text{ \AA}$ , respectively. Given the typical  $\text{EW}(\text{Ly}\alpha)$  of  $73 \text{ \AA}$  estimated from the narrow-band photometry in the VIMOS-LAEs sample, we consider the red spectrum using Eq. (1) to be the more accurate prescription. Additionally, the sought-after diagnostic UV lines of  $\text{C III]}$ ,  $\text{C IV}$ , and  $\text{O III]}$  are detected with greater significance in the red composite spectrum, whilst the noise level around these emission lines is greater in the black spectrum. Figure 4 thus demonstrates that the prescription of Eq. (1) is preferred for the  $\Delta v_{\text{Ly}\alpha}$  estimation from  $\text{EW}(\text{Ly}\alpha)$ , especially for LAEs with a large EW.

To evaluate sample variance and statistical noise, we adopt a bootstrap technique, similar to that used in [Shapley et al. \(2003\)](#). We generated 1000 fake composite spectra constructed from the sample of spectra used in creating the real composite spectra. Each fake spectrum was constructed in the same way, with the same number of spectra as the actual composite, but with the list of input spectra formulated by selecting spectra at random, with replacement, from the full list of VIMOS LAE spectra. With these

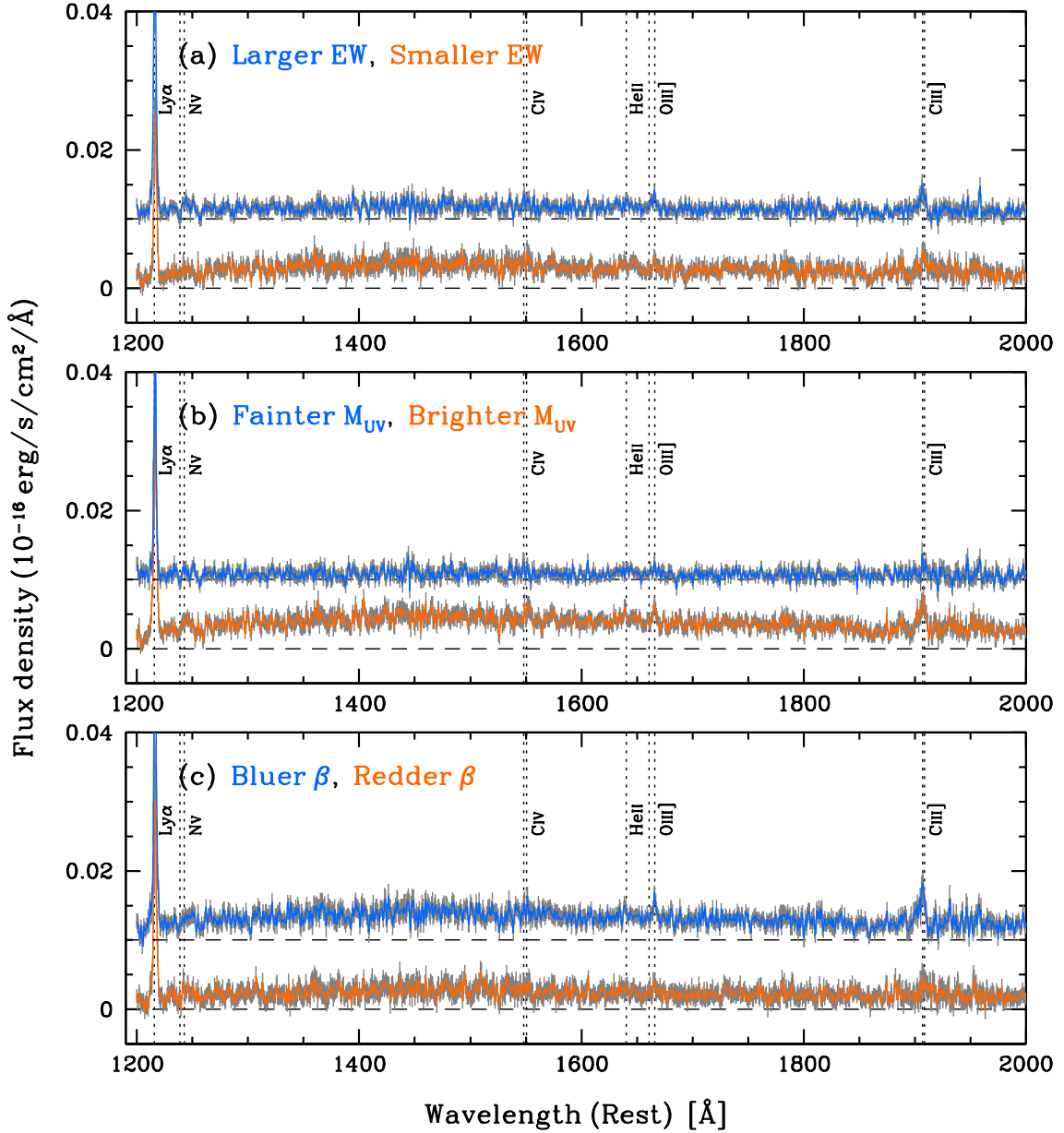


**Figure 5.** Composite rest-frame spectra of the VIMOS LAEs separated according to the strength of (a)  $\text{EW}(\text{Ly}\alpha)$ , (b)  $M_{\text{UV}}$ , and (c) UV slope  $\beta$ . In each case the smaller/fainter and larger/brighter subsamples are displayed in blue/orange respectively in each panel. For convenience the blue spectrum is offset vertically. The grey shaded region around each spectrum refers to the standard deviation of the flux density at each wavelength estimated by bootstrap resampling (see text for details). The wavelengths of key diagnostic emission lines are marked with a dotted line.

1000 fake spectra, we derived the standard deviation at each dispersion pixel. The standard deviations are taken into account in the following analyses based on line fluxes and EWs.

### 3.2.1 Dependencies

To examine spectroscopic trends in the LAE sample, we now split the dataset into various subsamples based on the properties of the individual spectra. Since most of the LAEs are faint, we simply divide the sample into two halves to maximise the S/N of the resulting composite spectra. We chose the key properties of the  $\text{EW}(\text{Ly}\alpha)$ , absolute UV magnitude

$M_{\text{UV}}$ , and UV continuum slope  $\beta$  to investigate the various trends. The median and the threshold values are  $\text{EW}(\text{Ly}\alpha) = 73 \text{ \AA}$ ,  $M_{\text{UV}} = -19.5$ , and  $\beta = -1.50$ . Note that the subsamples selected according to the UV slope are somewhat smaller since some LAEs lack the necessary multiple bands of rest-frame photometry. The composite spectra of the subsamples are shown in Figure 5, and the various properties derived from the composite spectra are listed in Table 3. The errors on these entries take into account the variance measure on the stacked spectra as detailed above.

We begin by discussing Figure 6 which presents the correlation between  $\text{EW}(\text{Ly}\alpha)$  and  $\text{EW}(\text{CIII})$  for the subsam-

**Table 3.** Spectroscopic properties of subsamples

	Smaller EW(Ly $\alpha$ )	Larger EW(Ly $\alpha$ )	Brighter $M_{UV}$	Fainter $M_{UV}$	Redder $\beta$	Bluer $\beta$
$N_{\text{gal}}$	35	35	35	35	25	26
$\langle \text{EW}(\text{Ly}\alpha) \rangle$	38.	119.	40.	113.	42.	63.
$\langle M_{UV} \rangle$	-20.00	-19.20	-20.32	-18.97	-19.72	-19.69
$\langle \beta \rangle$	-1.5	-2.3	-1.5	-3.3	-1.2	-2.0
CIV EW	$1.41 \pm 0.53$	$2.91 \pm 0.77$	$1.75 \pm 0.45$	$3.88 \pm 1.18$	$< 1.57$	$1.61 \pm 0.47$
CIV/CIII]	$0.36 \pm 0.16$	$0.29 \pm 0.09$	$0.30 \pm 0.08$	$0.49 \pm 0.19$	$< 0.39$	$0.22 \pm 0.07$
CIV/CIII] <sub>corr</sub> <sup>(†)</sup>	$0.46 \pm 0.20$	$0.32 \pm 0.09$	$0.38 \pm 0.11$	$0.49 \pm 0.19$	$< 0.54$	$0.25 \pm 0.08$
HeII EW	$1.15 \pm 0.35$	$1.83 \pm 0.45$	$1.26 \pm 0.30$	$2.03 \pm 0.53$	$1.12 \pm 0.34$	$1.52 \pm 0.38$
HeII EW <sub>corr</sub> <sup>(‡)</sup>	$0.15 \pm 0.05$	$0.83 \pm 0.26$	$0.26 \pm 0.08$	$1.03 \pm 0.34$	$0.11 \pm 0.04$	$0.51 \pm 0.17$
HeII/CIII]	$0.26 \pm 0.10$	$0.19 \pm 0.05$	$0.20 \pm 0.05$	$0.26 \pm 0.09$	$0.22 \pm 0.09$	$0.19 \pm 0.05$
HeII/CIII] <sub>corr</sub> <sup>(†)(‡)</sup>	$0.039 \pm 0.020$	$0.089 \pm 0.038$	$0.050 \pm 0.020$	$0.130 \pm 0.062$	$0.029 \pm 0.016$	$0.073 \pm 0.031$
O III] EW	$1.89 \pm 0.66$	$4.67 \pm 0.87$	$1.99 \pm 0.30$	$3.60 \pm 1.32$	$1.68 \pm 0.41$	$2.95 \pm 0.36$
O III]/CIII]	$0.42 \pm 0.17$	$0.45 \pm 0.10$	$0.31 \pm 0.06$	$0.39 \pm 0.17$	$0.34 \pm 0.12$	$0.37 \pm 0.07$
O III]/CIII] <sub>corr</sub> <sup>(†)</sup>	$0.49 \pm 0.20$	$0.47 \pm 0.11$	$0.36 \pm 0.07$	$0.39 \pm 0.17$	$0.41 \pm 0.15$	$0.41 \pm 0.07$
CIII] EW	$5.41 \pm 1.20$	$15.14 \pm 1.99$	$9.17 \pm 0.98$	$11.05 \pm 2.62$	$5.89 \pm 1.57$	$10.99 \pm 1.41$

(†) Corrected for reddening. (‡) Corrected for the HeII stellar emission (§3.2.2).

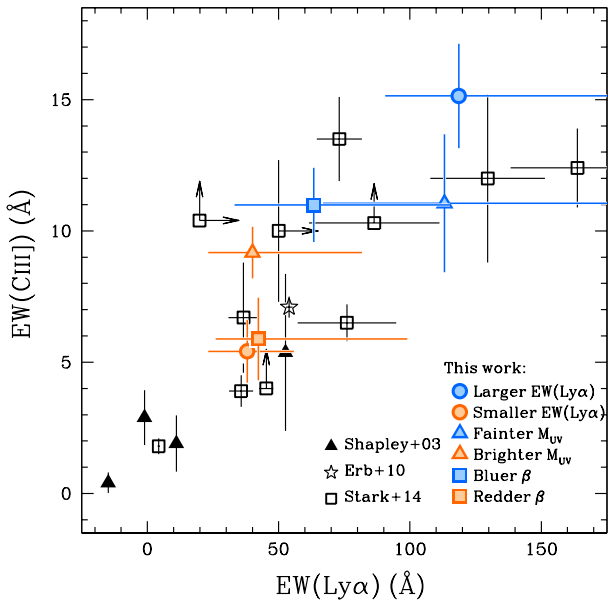


**Figure 6.** Relationship between EW(Ly $\alpha$ ) and EW(CIII]) for the VIMOS and other samples. The blue and orange filled symbols show the composites of the six VIMOS subsamples as indicated in the legend. The black symbols refer to measures for  $z = 2 - 3$  galaxies compiled from the literature as described in the legend.

ples. A clear trend is obvious and follows that previously reported (Stark et al. 2014; Rigby et al. 2015; Le Fèvre et al. 2017). CIII] emission is stronger in LAEs with larger EW(Ly $\alpha$ ), fainter  $M_{UV}$ , and bluer UV slopes. Similar trends are also observed in CIV, O III], and HeII emission (corrected; §3.2.2). As clarified by earlier studies with photoionisation models (Jaskot & Ravindranath 2016; Nakajima et al. 2017), simple stellar populations find it hard to reproduce

CIII] with EW  $\gtrsim 10$  Å and populations including the contribution of massive binary systems have been proposed (§4).

### 3.2.2 Corrections to the nebular spectra

To ensure the intrinsic nebular spectra of the VIMOS LAEs can be directly compared with photoionisation models (§ 3.3), we must apply several corrections to the observed UV spectra.

Firstly, we need to correct for the contribution of stellar emission. The HeII emission line is a composite of both stellar and nebular emission (e.g. Brinchmann et al. 2008; Erb et al. 2010; Steidel et al. 2016). Since our VIMOS data do not have the spectral resolution necessary to resolve the two components, we use a stellar synthesis code to predict the stellar contribution and hence subtract it. We use publicly available BPASS (v2.0; Stanway et al. 2015) SEDs including binary evolution to predict the stellar HeII emission strengths. Considering a current star-formation age of 10 to several 100 Myr as plausible for LAEs (e.g. Gawiser et al. 2006, 2007; Ono et al. 2010; Kusakabe et al. 2018), the stellar HeII emission is predicted to have EW  $\approx 0.8 - 1.4$  Å<sup>2</sup>. As a fiducial value, we adopt a value of  $1.0 \pm 0.2$  Å, as used by Nakajima et al. (2017). We consider this appropriate for a sub-solar metallicity of  $Z \approx 0.2 - 0.5 Z_{\odot}$  (e.g., Nakajima et al. 2013; Trainor et al. 2016). If a lower metallicity were assumed, the stellar HeII emission could be slightly larger,  $1.2 \pm 0.2$  Å.

A further correction is required for dust reddening. In Paper I we assumed such a correction is negligible for LAE.

<sup>2</sup> The stellar HeII emission strength is estimated to be EW  $\approx 0.8 - 1.2$  Å if we adopt the v2.1 BPASS models (Eldridge et al. 2017). Our results are thus not affected by the choice between v2.0 and v2.1. In this paper, we use the v2.0 BPASS models which are also adopted in the photoionisation models of Nakajima et al. (2017) (§3.3).



Here, in an improvement, we utilise the UV slope  $\beta$  obtained from the Subaru photometry in conjunction with our stellar population models. Using the SMC extinction curve and the BPASS SEDs (Reddy et al. 2018), we correct for the reddening of the line ratios for each of the six subsamples using the median value of  $\beta$ . The corrections are small and do not affect our results significantly. As an example, for the subsample with weaker  $\text{EW}(\text{Ly}\alpha)$   $\beta \approx 1.5$  and the corrected  $\text{CIV}/\text{CIII}]$  ratio (which spans the widest wavelength range we use) is increased by a factor of  $\sim 1.3$  which is within the  $1\sigma$  uncertainties. Although it is debatable whether nebular emission and the stellar continuum suffer the same amount of dust attenuation (e.g. Reddy et al. 2015), such differences will not be a concern for measures based on EWs.

### 3.3 UV diagnostic diagrams

Following the corrections adopted in §3.2.2, we now proceed to interpret the UV spectra of our various VIMOS subsamples using three UV diagnostic emission line ratios in Figure 7. Since these are high ionisation lines, UV line diagnostics such as  $\text{CIII}]$ ,  $\text{CIV}$  and  $\text{HeII}$  were initially applied to spectra of radio galaxies and AGNs (e.g., Villar-Martín et al. 1997; Allen et al. 1998; Groves et al. 2004; Nagao et al. 2006; Dors et al. 2014). There is now broader interest in studying these lines to gauge the ionisation field in star-forming galaxies, both theoretically (e.g., Feltre et al. 2016; Gutkin et al. 2016; Nakajima et al. 2017) and observationally (e.g., Stark et al. 2014; Amorín et al. 2017; Le Fèvre et al. 2017). Our goal is to derive the physical properties of the gaseous phase in the interstellar medium (ISM) in the context of the hardness of the ionising spectrum, as characterised by  $\xi_{\text{ion}}$  – the number of Lyman continuum photons per UV luminosity.

In the following we follow the procedures introduced by Nakajima et al. (2017). In that work UV diagnostic diagrams are interpreted with photoionisation models which include incident radiation fields of both stellar populations and AGN and cover a wide range of metallicities and ionisation parameters. The authors demonstrate how such diagrams can be used not only to separate star-forming galaxies from AGN but also to constrain  $\xi_{\text{ion}}$  for star-forming galaxies. Fortunately, as expected, Figure 7 demonstrates that all of our various LAE subsamples are consistent with star-forming regions. Thus, in the following, we only use the stellar photoionisation models to discuss their properties. We briefly describe the details of the stellar photoionisation models below.

Our stellar photoionisation models are based on CLOUDY (version 13.03; Ferland et al. 1998, 2013) and assume constant density homogeneous inter-stellar gas with a plane-parallel geometry. Dust physics and elemental depletion factors follow the analyses of Dopita et al. (2006) and Nagao et al. (2011). All elements except nitrogen, carbon and helium are taken to be primary nucleosynthesis elements. For carbon and nitrogen, we use the formalism of Dopita et al. (2006) and López-Sánchez et al. (2012), respectively, to account for their secondary products. For helium, we adopt the form given by Dopita et al. (2006). The photoionisation models are calculated by varying the metallicity and ionisation parameter, fixing the gas density  $n_{\text{H}} = 10^2 \text{ cm}^{-3}$ . For the radiation field, we adopt the popu-

lation synthesis code BPASS (v2.0; Stanway et al. 2015) for binary star populations and POPSTAR (Mollá et al. 2009) for single stellar populations. Stellar metallicities are matched to their gas-phase equivalents. We assume a constant star-formation history and vary the duration of current star-formation from 1 to 1000 Myr. An older age corresponds to a lower  $\xi_{\text{ion}}$  parameter. Emission line ratios are insensitive to the duration of star-formation, but the EWs of UV lines are affected as the continuum level strongly depends on the older stellar population. The advantage of using the models of Nakajima et al. (2017) is that they predict EWs of the UV lines as a function of metallicity, ionisation parameter, and  $\xi_{\text{ion}}$ .

We evaluate the average ionisation parameter and metallicity by fitting stellar photoionisation models to the most sensitive line ratios of  $\text{CIV}/\text{CIII}]$  and  $(\text{CIII}]+\text{CIV})/\text{HeII}$ . The estimation procedure is similar to that typically adopted for the optical  $[\text{O III}]/([\text{O II}]+([\text{O II}]+[\text{O III}]))/\text{H}\beta$  diagram (e.g. Kewley & Dopita 2002; Kobulnicky & Kewley 2004; Nakajima & Ouchi 2014) but here applied to more highly ionised nebular regions. The  $(\text{CIII}]+\text{CIV})/\text{HeII}$  is sensitive to metallicity and increases toward a higher metallicity. This is because of (i) an increase of carbon element and (ii) a softening of the radiation field (i.e., a weakening of the  $\text{HeII}$  emission) with increasing metallicity. The  $\text{CIV}/\text{CIII}]$  is mainly governed by the ionisation parameter and increases with it. Moreover, the  $(\text{CIII}]+\text{CIV})/\text{HeII}$  ( $\text{CIV}/\text{CIII}]$ ) ratio also has a weak dependency on the ionisation parameter (metallicity). We therefore use both the ratios of  $(\text{CIII}]+\text{CIV})/\text{HeII}$  and  $\text{CIV}/\text{CIII}]$  to estimate the metallicity and ionisation parameter simultaneously. The top left panel of Figure 7 shows that LAEs with larger  $\text{EW}(\text{Ly}\alpha)$ , fainter  $M_{\text{UV}}$ , and bluer UV slopes (hereafter called the “stronger LAEs sample”) tend to present a smaller  $(\text{CIII}]+\text{CIV})/\text{HeII}$  ratio. This indicates that the stronger LAEs sample has a lower gas-phase metallicity – a result that would not be affected if we adopted a stronger correction for stellar emission of  $\text{EW}(\text{HeII})_{\text{stellar}} = 1.2 \pm 0.2 \text{ \AA}$  (§3.2.2). Based on the binary stellar population photoionisation models, the stronger LAEs sample has an average metallicity of  $Z \approx 0.05 - 0.2 Z_{\odot}$ , while the weaker LAEs sample has a somewhat higher metallicity of  $Z \approx 0.1 - 0.5 Z_{\odot}$ . The ionisation parameters  $U$  – defined as the ratio of the ionising photon flux to the gas density – are constrained at the same time, differ with  $\log U \approx -1.5$  to  $-2.2$  for the stronger LAEs sample compared to  $\log U \approx -2.0$  to  $-2.5$  for the weaker LAEs sample. We derive the best-fit and  $1\sigma$  uncertainty of metallicity and ionisation parameter for each of the three sub-samples in the stronger and weaker LAEs samples. The ranges of the properties above are given to cover the properties of the three sub-samples including the  $1\sigma$  uncertainties. Although the subsample of LAEs with the redder UV slope does not exhibit a significant  $\text{CIV}$  detection, its relatively large  $\text{EW}(\text{CIII}]$  ensures that its ionisation parameter could not be less than  $\log U \approx -2.5$ . These quantities are not significantly altered if we adopt the single stellar population models.

One uncertainty in the analysis is the use of  $\text{CIV}$  as a diagnostic tool. Since  $\text{CIV}$  line photons can be trapped in a highly ionised nebular region by resonant scattering, they would be preferentially absorbed and weakened by internal dust. Although dust physics is included in the modelling, there remain uncertainties in accurately modelling how this

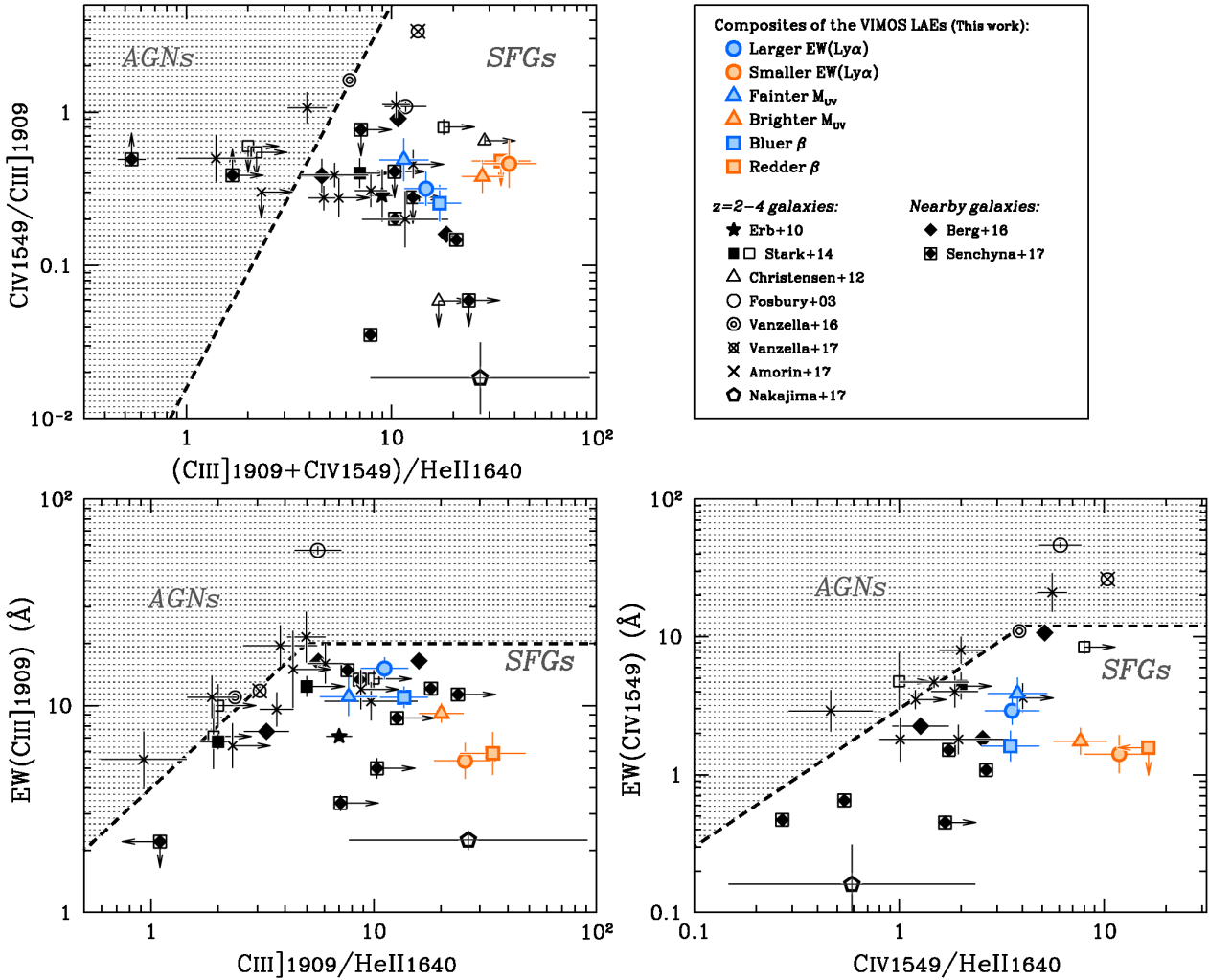


**Figure 7.** Diagnostic diagrams involving various UV emission line ratios: CIV/CIII] vs. (CIII]+CIV)/HeII (top left), EW(CIII] vs. CIII]/HeII (bottom left), and EW(CIV) vs. CIV/HeII (bottom right). Blue and orange symbols present the six VIMOS subsamples as shown in the legend. The black symbols are  $z = 0-4$  star-forming galaxies compiled from the literature by Nakajima et al. (2017), as shown in the legend. In these diagrams, star-forming galaxies can be separated from AGNs, which are dominated in the grey hatched areas (see Nakajima et al. 2017).

affects CIV emission. For this work, we find that the LAEs are on average fairly free from dust with  $E(B-V) = 0.09 \pm 0.07$  (§2.1) and so assume CIV measures will not be severely affected.

It is important to note that these models also reproduce our O III] emission line strengths. Since the stellar photoionisation models of Nakajima et al. (2017) by default assume an empirical relationship between C/O and O/H ratios (Dopita et al. 2006) to give a carbon abundance at each metallicity, LAEs are on average expected to obey the same relationship, as typically inferred for continuum-selected galaxies at similar redshifts (e.g. Steidel et al. 2016). Using the method of Pérez-Montero & Amorín (2017), the C/O ratios are estimated from the (CIII]+CIV)/O III] ratios to be  $\log C/O \approx -0.7 \pm 0.1$ .

### 3.4 The Hardness of the Ionising Spectrum

Finally, with the knowledge of the metallicity and ionisation parameter  $U$ , we turn to estimating the hardness of the ionising spectrum,  $\xi_{ion}$ . We consider both the EW(CIII]) and EW(CIV) diagnostic diagrams presented in the two lower panels of Figure 7.

The strength of the various UV lines is sensitive not only to the ISM condition but also to the ratio of the number of ionising photons to the (non-ionising) UV continuum, i.e.,  $\xi_{ion}$ . The UV nebular continuum must also be considered for an accurate analysis. Using the derived ISM properties (§3.3) and assuming a constant star-formation rate, we vary the duration of current star-formation from 1 to 1000 Myr in order to match the observed EWs of CIII] and CIV. The inferred age can then be directly translated into a constraint on  $\xi_{ion}$ . It is important to note that in the following derivation of  $\xi_{ion}$  we will follow the convention of assuming a zero escape fraction of ionising photons (see discussion in §4).

The derivation of  $\xi_{ion}$  also depends on whether or not

**Table 4.** Summary of the inferred properties of the VIMOS LAEs with the UV lines.

Sample	Input radiation	$Z (Z_{\odot})$	$\log U$	Age (Myr)	$\log \xi_{\text{ion}}/\text{erg}^{-1} \text{ Hz}$
Stronger LAEs	<i>(Subsamples of larger <math>EW(\text{Ly}\alpha)</math>, fainter <math>M_{\text{UV}}</math>, bluer UV slope)</i>				
	binary stellar pop.	$0.05 \cdots 0.2$	$-2.2 \cdots -1.5$	$\lesssim 20$	$25.68 \pm 0.13$
Weaker LAEs	<i>(Subsamples of smaller <math>EW(\text{Ly}\alpha)</math>, brighter <math>M_{\text{UV}}</math>, redder UV slope)</i>				
	binary stellar pop.	$0.1 \cdots 0.5$	$-2.5 \cdots -2.$	$10 \cdots 500$	$25.54 \pm 0.09$

the stellar population includes binary stars. As clarified by Nakajima et al. (2017), EWs of CIII] and CIV generated by a single stellar population produce  $EW(\text{CIII])} \lesssim 12 \text{ \AA}$  and  $EW(\text{CIV}) \lesssim 9 \text{ \AA}$ , whereas binary stellar populations yield EWs as large as  $\sim 20 \text{ \AA}$  and  $\sim 12 \text{ \AA}$ , respectively (see also Jaskot & Ravindranath 2016). Since the stronger LAEs sample shows  $EW(\text{CIII])}$ s of  $\approx 13 \text{ \AA}$ , a single stellar population is likely insufficient. We therefore adopt the binary stellar population models for the stronger LAEs sample.

After some consideration, we decided to focus on using the  $EW(\text{CIII])}$  figure (lower left in Figure 7 to estimate  $\xi_{\text{ion}}$ . There remains a concern that the CIV measurements may be affected by underlying stellar absorption. For the stronger LAEs sample, the large  $EW(\text{CIII])}$  is consistent with a young star-formation age and a high  $\xi_{\text{ion}}$ . The inferred age spans a few Myr in the lowest metallicity case ( $Z \approx 0.05 Z_{\odot}$ ) to  $\sim 20 \text{ Myr}$  at  $Z \approx 0.2 Z_{\odot}$ . The resulting average value of  $\xi_{\text{ion}}$  is then  $\log \xi_{\text{ion}}/\text{erg}^{-1} \text{ Hz} \approx 25.68 \pm 0.13$ . This error includes the uncertainties of the  $EW(\text{CIII])}$ s as well as those of the inferred ISM properties (§3.3). Likewise, the weaker LAEs sample is diagnosed to have a current star-formation age of  $\sim 10$  to  $500 \text{ Myr}$  and  $\log \xi_{\text{ion}}/\text{erg}^{-1} \text{ Hz} \approx 25.54 \pm 0.09$  if the binary stellar population models are assumed. The difference between the two samples arises primarily from the different CIII] EWs.

One uncertainty in interpreting  $\xi_{\text{ion}}$  for the weaker LAEs sample is whether or not to include binary stars in the stellar population. If we adopt the single star models, the star-formation age is significantly reduced to  $\sim 1 - 7 \text{ Myr}$  with  $\log \xi_{\text{ion}}/\text{erg}^{-1} \text{ Hz} \approx 25.5 - 25.7$ . The younger age arises from the fact that (i) single star models predict a smaller maximum EW of CIII], and (ii)  $EW(\text{CIII])}$  weakens more rapidly whereas binary evolution prolongs the period during which blue stars dominate the spectrum (see also Nakajima et al. 2017). It is unlikely, however, that the weaker LAEs population is so young (cf. Gawiser et al. 2006, 2007; Ono et al. 2010; Guaita et al. 2011; Kusakabe et al. 2018) and indeed even younger than the stronger LAEs population. We note that typical ages inferred for the LBG population at similar redshifts are several  $\times 100 \text{ Myr}$  (e.g. Reddy et al. 2012; Nakajima et al. 2017) where binary star models are preferred. Since the weaker LAEs can logically be considered to represent a population intermediate between LBGs and the stronger LAEs (e.g., Steidel et al. 2016; Trainor et al. 2016; Nakajima et al. 2017), it seems reasonable to include binary stars.

The ISM properties and  $\xi_{\text{ion}}$  derived from the comparison of the UV emission lines with the photoionisation models of Nakajima et al. (2017) are given in Table 4. The uncer-

tainties on  $\xi_{\text{ion}}$  reflect both the variance arising from the use of stacked spectra and the range of ages considered.

## 4 DISCUSSION

We present VIMOS measurements of the rest-frame UV nebular emission lines of CIII], CIV, HeII, and OIII] drawn from a sample of 70  $z = 3.1$  LAEs. By dividing the sample into nearly equal subsets based on the  $EW(\text{Ly}\alpha)$ , UV magnitude  $M_{\text{UV}}$ , and UV slope  $\beta$ , we demonstrate that the “stronger LAEs sample” with larger  $EW(\text{Ly}\alpha)$ , fainter  $M_{\text{UV}}$  and bluer  $\beta$  have stronger EWs of CIII] emission and smaller (CIII]+CIV)/HeII line ratios than the corresponding “weaker LAEs sample”.

Using our photoionisation models and the UV diagnostic diagrams presented in Nakajima et al. (2017), we interpret these trends as indicating that the stronger LAEs sample, which represents the more intense LAE phenomenon, has typically a lower gas phase metallicity and, importantly, a more efficient production of ionising photons. In addition to inferring a higher  $\xi_{\text{ion}}$ , binary stars are essential in our modelling to reproduce the EWs of CIII].

We can place our results in context by examining, in Figure 8, the distribution of  $\xi_{\text{ion}}$  as a function of  $M_{\text{UV}}$  for the two subsamples of the VIMOS LAEs as well as for other high redshift sources, including the modest sample of LAEs studied with MOSFIRE in Paper I for which  $\xi_{\text{ion}}$  was inferred from  $H\beta$  using recombination theory. We also include various  $z \approx 5 - 8$  galaxies (Stark et al. 2015b, 2017; Matthee et al. 2017; Harikane et al. 2017) for comparison purposes including several exploiting CIII] emission, and continuum-selected LBGs at  $z = 2 - 5$  (Bouwens et al. 2016; Nakajima et al. 2017; Shivaei et al. 2018). The  $\xi_{\text{ion}}$  parameters of Stark et al. (2015b, 2017) and Nakajima et al. (2017) are based on the UV emission lines with photoionisation models as we adopt in this paper, while the other studies estimate  $\xi_{\text{ion}}$  from hydrogen recombination lines.

Over the UV magnitude range from  $M_{\text{UV}} \approx -19.5$  to  $-22.5$ , the continuum-selected LBGs at  $z = 2 - 5$  show a uniform value,  $\log \xi_{\text{ion}}/\text{erg}^{-1} \text{ Hz} \approx 25.2 - 25.4$ . On the other hand, LAEs have a consistently larger value by  $\sim 0.2 - 0.3$  dex, as originally claimed from a much smaller sample in Paper I. Our analysis has also shown that UV faint LAEs present a higher  $\xi_{\text{ion}}$  than their luminous counterparts.

The most intriguing comparison is with the emerging data in the reionisation era. Although the uncertainties remain large, and the samples modest in size, the large values of  $\xi_{\text{ion}}$  inferred for the faintest metal-poor VIMOS LAEs are similar to those observed in galaxies at  $z > 6$  (Stark et al.

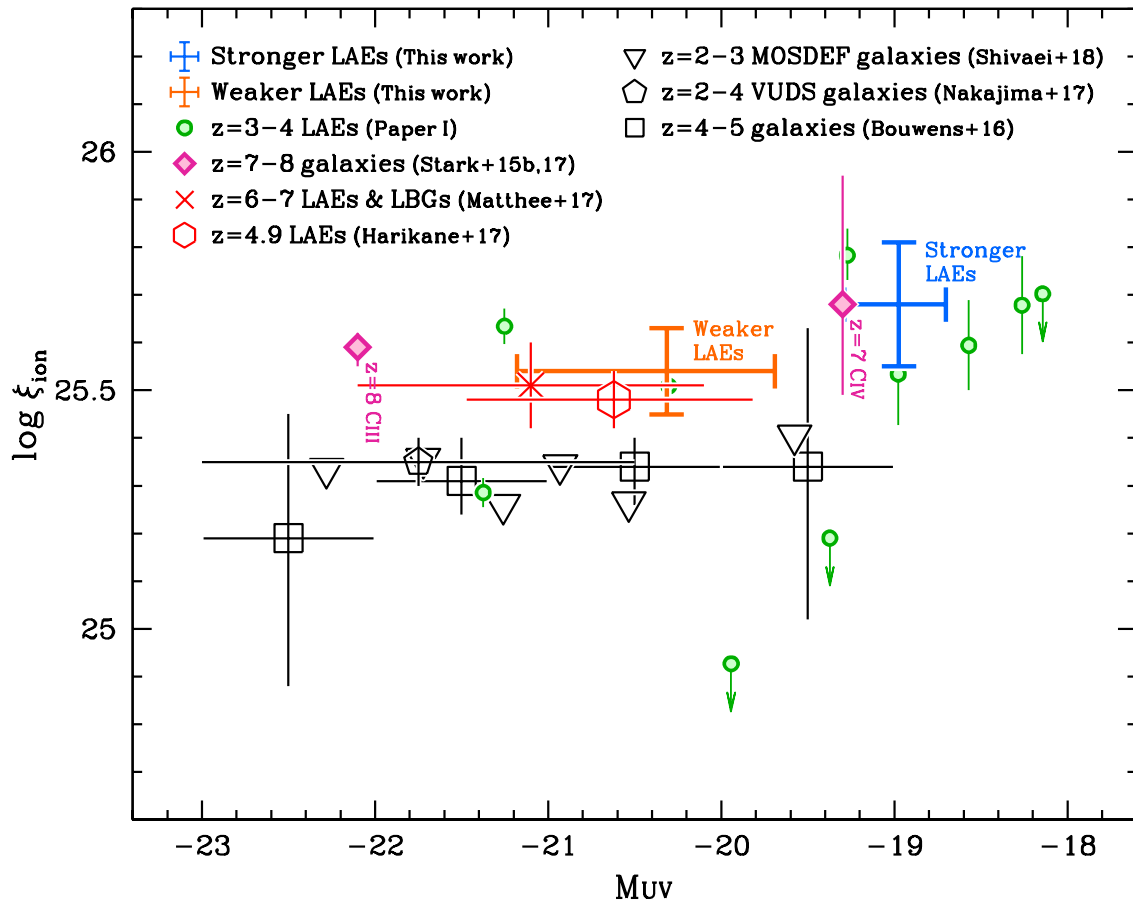


**Figure 8.** The efficiency of ionising photon production  $\xi_{\text{ion}}$  as a function of UV absolute magnitude. Blue and orange refer to the stronger and the weaker LAEs samples respectively. Green circles are individual LAEs whose  $\xi_{\text{ion}}$  were derived from  $H\beta$  measures and recombination theory (Paper I). Among the 13 LAEs presented in Paper I, one AGN-LAE and two LAEs whose  $\xi_{\text{ion}}$  is less reliable are not displayed. Magenta diamonds present a  $z = 7.05$  galaxy identified with CIV (Stark et al. 2015b) and a  $z = 7.73$  galaxy identified with CIII] (Stark et al. 2017). Red crosses represents a compilation of  $z = 6-7$  luminous Ly $\alpha$ -selected and UV-selected galaxies (Matthee et al. 2017), and the red hexagon is an average for LAEs at  $z = 4.9$  (Harikane et al. 2017). Black open symbols show larger samples of continuum-selected Lyman break galaxies at similar redshifts; from MOSDEF (inverse triangles; Shivaei et al. 2018; at  $z = 1.4-2.6$ ), VUDS (pentagon; Nakajima et al. 2017; at  $z = 2-4$ ; see also Le Fèvre et al. 2015, 2017), and Bouwens et al. (2016) (squares; at  $z = 3.8-5.0$ ). An SMC attenuation law is adopted in the correction for dust reddening.  $\xi_{\text{ion}}$  values are calculated under the assumption of a zero escape fraction of ionising photons excepting for those from MOSDEF which refer to an assumed value of 9% (see text for details).

2015b, 2017; Matthee et al. 2017; Harikane et al. 2017). Since our LAEs likewise present intense [O III] $\lambda\lambda 5007, 4959$  emission (Paper I) as inferred indirectly from *Spitzer*/IRAC photometry for  $z > 6$  star-forming galaxies (Smit et al. 2014, 2015; Oesch et al. 2015; Roberts-Borsani et al. 2016; Harikane et al. 2017), we conclude they remain valuable low-redshift analogues of the possible sources of cosmic reionisation.

In order to understand the physical origin of the intense CIII] and Ly $\alpha$  emission which combine to define the ‘stronger LAE sample’ as illustrated in Figure 6, we present in Figure 9 the distribution of EW(CIII]) as a function of metallicity. Here we compare data from our two VIMOS-LAEs sub-samples with other relevant galaxies compiled from the literature.

It is clear from Figure 9 that galaxies with a lower metallicity present a larger EW CIII]. One reason is that CIII] EW peaks at sub-solar metallicities, as shown with the photoionisation models. Another arises because the ionisation

parameter becomes higher at lower metallicity. EW(CIII]) increases with ionisation parameter for a given metallicity up to  $\log U \simeq -2$ . As emphasised earlier, binary stellar populations can also produce stronger EWs of CIII] than single stellar populations at a fixed ISM properties (Nakajima et al. 2017), although it seems likely binary stellar populations are an ubiquitous feature of early star-forming galaxies.

The other important parameter governing the EW(CIII]) is  $\xi_{\text{ion}}$ , or the age of the current star-formation. The photoionisation models in Figure 9 are based on 1 Myr old stellar populations providing a maximal EW(CIII]) for a given ISM condition. Weaker EWs correspond to longer star-formation ages and lower  $\xi_{\text{ion}}$ .

Finally we issue some caveats. The most important variable that could change our  $\xi_{\text{ion}}$  estimates is the escape fraction of ionising photons. EWs of CIII] and CIV would be weakened with a higher escape fraction for a fixed ISM condition, since less ionising photons are necessary to produce the high ionisation lines (see also



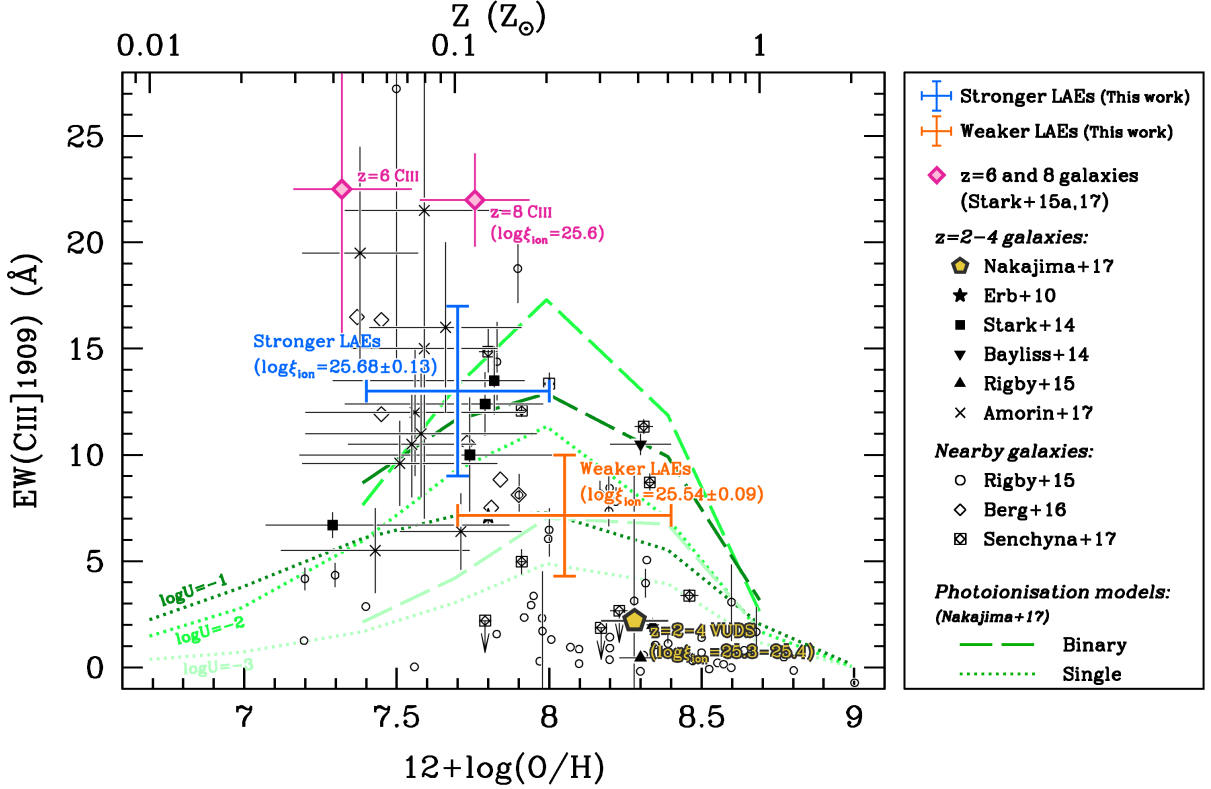


**Figure 9.** The  $\text{EW}(\text{C III]})$  as a function of metallicity. The stronger and weaker LAEs sample are indicated by the blue and orange error bars, respectively. The magenta symbol present the  $z = 7.73$  galaxy identified with  $\text{C III]}$  (Stark et al. 2017), and the black symbols represent  $z = 0 - 4$  galaxies compiled from the literature as shown in the legend. The average LBG population at  $z = 2 - 4$  drawn from VUDS (Nakajima et al. 2017) for which a  $\xi_{\text{ion}}$  measurement is available is highlighted in yellow. Green curves present photoionisation models using single- (dotted) and binary- (long dashed) stellar populations (Nakajima et al. 2017) and trace the maximum EW for a given metallicity and a range of ionisation parameters:  $\log U = -1$  (dark green),  $-2$  (green), and  $-3$  (light green).

Jaskot & Ravindranath 2016). For example, based on the models of Jaskot & Ravindranath (2016), for galaxies with a sub-solar metallicity, an ionisation parameter of  $\log U \approx -2.5$ , and a 20% escape fraction would lower the EW of  $\text{C III]}$  by a factor of  $\lesssim 1.3$  as compared with the zero escape fraction case. However, in the specific case of the MOSDEF survey of LBGs (Shivaei et al. 2018) where an escape fraction of 9% was typically assumed, applying a correction to our adopted value of zero would only raise those points by  $\approx 0.04$  dex in Figure 8 and not change our conclusions. Inevitably until we can independently examine the Lyman continuum leakage from our sample, we cannot quantitatively break this degeneracy and determine an absolute  $\xi_{\text{ion}}$ .

A further issue is the fact our photoionisation models predict that the  $\text{C III]}$  EW decreases if the metallicity becomes very much lower due to the lack of carbon. Presumably, the positive correlation between EWs of  $\text{Ly}\alpha$  and  $\text{C III]}$  as shown in Figure 6 indicates such systems have not yet been detected (see also Nakajima et al. 2017; Harikane et al. 2017).

Furthermore the C/O abundance ratio could affect the interpretation. By default our photoionisation models assume the empirical relationship between C/O and O/H ratios (Dopita et al. 2006) to predict the carbon lines strength. As discussed earlier, we have confirmed with  $(\text{C III]} + \text{C IV})/\text{O III]}$  ratios that our VIMOS-LAEs typically

have C/O ratios of  $\log \text{C/O} \approx -0.7 \pm 0.1$  and follow the empirical relation. However, this may not be true for higher- $z$  galaxies. Indeed, the  $\text{C III]}$ -or- $\text{C IV}$  emitting galaxies at  $z = 7 - 8$  studied by Stark et al. (2015a,b, 2017) have best-fit C/O ratios higher than expected from the empirical relation by  $\sim 0.1 - 0.4$  dex. Although the constraints are very weak for these high- $z$  objects with the limited data, their large EWs of  $\text{C III]}$  for their low metallicities, as presented in Figure 9, would result from their elevated C/O ratios. The physical cause of such high C/O abundance ratios is unclear (see e.g., Mattsson 2010; Berg et al. 2016; Nakajima et al. 2017 for a discussion).

In summary, therefore, the more intense LAEs with strong  $\text{C III]}$  studied here and, by reference to Paper I, those with intense  $[\text{O III}]$ , can be considered to be young metal-poor galaxies in an early phase of galaxy evolution, providing a large amount of ionising photons into the ISM to achieve highly ionised nebular regions. They remain excellent analogues of galaxies in the reionisation era and, by virtue of their relative proximity and brightness, valuable targets for further detailed study.

### Acknowledgements

We acknowledge financial support from European Research Council Advanced Grant FP7/669253 (TF, RSE). KN acknowledges a JSPS Overseas Research Fellowship. BER is supported in part by the program HST-GO-14747 provided

by NASA through a grant from the Space Telescope Science Institute, which is operated by the Association of Universities for Research in Astronomy, Incorporated, under NASA contract NAS5-26555. It is a pleasure to thank Dan Stark, Masami Ouchi, Daniel Schaerer and the anonymous referee for useful comments and discussions. We also thank T. Hayashino, T. Yamada, Y. Matsuda and A. K. Inoue for providing the LAE catalogue and the photometric data. The work is based on data products from observations made with ESO Telescopes at the La Silla Paranal Observatory under ESO programme ID 098.A-0010(A). Further data was taken with the W.M. Keck Observatory on Maunakea, Hawaii which is operated as a scientific partnership among the California Institute of Technology, the University of California and the National Aeronautics and Space Administration. This Observatory was made possible by the generous financial support of the W. M. Keck Foundation. The authors wish to recognise and acknowledge the very significant cultural role and reverence that the summit of Maunakea has always had within the indigenous Hawaiian community. We are most fortunate to have the opportunity to conduct observations from this mountain.

## REFERENCES

- Adelberger, K. L., Steidel, C. C., Shapley, A. E., & Pettini, M. 2003, *ApJ*, 584, 45
- Allen, M. G., Dopita, M. A., & Tsvetanov, Z. I. 1998, *ApJ*, 493, 571
- Amorín, R., Fontana, A., Pérez-Montero, E., et al. 2017, *NatAs*, 1, 0052
- Asplund, M., Grevesse, N., Sauval, A. J., & Scott, P. 2009, *ARA&A*, 47, 481
- Berg, D. A., Skillman, E. D., Henry, R. B. C., Erb, D. K., & Carigi, L. 2016, *ApJ*, 827, 126
- Bouwens, R. J., Smit, R., Labbé, I., et al. 2016, *ApJ*, 831, 176
- Brinchmann, J., Pettini, M., & Charlot, S. 2008, *MNRAS*, 385, 769
- Cassata, P., Tasca, L. A. M., Le Fèvre, O., et al. 2015, *A&A*, 573, A24
- Curtis-Lake, E., McLure, R. J., Pearce, H. J., et al. 2012, *MNRAS*, 422, 1425
- Dopita, M. A., Fischera, J., Sutherland, R. S., et al. 2006, *ApJS*, 167, 177
- Dors, O. L., Jr, Cardaci, M. V., Hägele, G. F., & Krabbe, Â. C. 2014, *MNRAS*, 443, 1291
- Eldridge, J. J., Stanway, E. R., Xiao, L., et al. 2017, *Publ. Astron. Soc. Australia*, 34, 58
- Erb, D. K., Pettini, M., Shapley, A. E., Steidel, C. C., Law, D. R., & Reddy, N. A. 2010, *ApJ*, 719, 1168
- Erb, D. K., Pettini, M., Steidel, C. C., Trainor, R. F., et al. 2014, *ApJ*, 795, 33
- Erb, D. K., Pettini, M., Steidel, C. C., et al. 2016, *ApJ*, 830, 52
- Feltre, A., Charlot, S., & Gutkin, J. 2016, *MNRAS*, 456, 3354
- Ferland, G. J., Korista, K. T., Verner, D. A., et al. 1998, *PASP*, 110, 761
- Ferland, G. J., Porter, R. L., van Hoof, P. A. M., et al. 2013, *RMxAA*, 49, 137
- Gawiser, E., van Dokkum, P. G., Growall, C., et al. 2006, *ApJ*, 642, L13
- Gawiser, E., Francke, H., Lai, K., et al. 2007, *ApJ*, 671, 278
- Groves, B. A., Dopita, M. A., & Sutherland, R. S. 2004, *ApJS*, 153, 75
- Guaita, L., Acquaviva, V., Padilla, N., et al. 2011, *ApJ*, 733, 114
- Gutkin, J., Charlot, S., & Bruzual, G. 2016, *MNRAS*, 462, 1757
- Harikane, Y., Ouchi, M., Shibuya, T., et al. 2017, arXiv e-prints, arXiv:1711.03735
- Hashimoto, T., Ouchi, M., Shimasaku, K., et al. 2013, *ApJ*, 765, 70
- Hayashino, T., Matsuda, Y., Tamura, H., et al. 2004, *AJ*, 128, 2073
- Inoue, A. K. & Iwata, I. 2008, *MNRAS*, 387, 1681
- Inoue, A. K., Shimizu, I., Iwata, I., & Tanaka M. 2014, *MNRAS*, 442, 1805
- Iwata, I., Inoue, A. K., Matsuda, Y., et al. 2009, *ApJ*, 692, 1287
- Izotov, Y. I., Orlitová, I., Schaerer, D., Thuan, T. X., Verhamme, A., Guseva, N. G., & Worseck, G. 2016a, *Nature*, 529, 178
- Izotov, Y. I., Schaerer, D., Thuan, T. X., Worseck, G., Guseva, N. G., & Orlitová, I., & Verhamme A. 2016b, *MNRAS*, 461, 3683
- Jaskot, A. E. & Ravindranath, S. 2016, *ApJ*, 833, 136
- Kewley, L. J., & Dopita, M. A. 2002, *ApJS*, 142, 35
- Kobulnicky, H. A., & Kewley, L. J. 2004, *ApJ*, 617, 240
- Kusakabe, H., Shimasaku, K., Ouchi, M., et al. 2018, *PASJ*, 70, 4
- Le Fèvre, O., Tasca, L. A. M., Cassata, P., et al. 2015, *A&A*, 576, A79
- Le Fèvre, O., Lemaux, B. C., Nakajima, K., et al. 2017, arXiv e-prints, arXiv:1710.10715
- Leitherer, C., Hernandez, S., Lee, J. C., & Oey, M. S. 2016, *ApJ*, 823, 64
- López-Sánchez, Á. R., Dopita, M. A., Kewley, L. J., Zahid, H. J., Nicholls, D. C., & Scharwächter, J. 2012, *MNRAS*, 426, 2630
- Madau, P. 1995, *ApJ*, 441, 18
- Matsuda, Y., Yamada, T., Hayashino, T., et al. 2004, *AJ*, 128, 569
- Matsuda, Y., Yamada, T., Hayashino, T., et al. 2005, *ApJ*, 634, L125
- Matthee, J., Sobral, D., Darvish, B., et al. 2017, *MNRAS*, 472, 772
- Mattsson, L. 2010, *A&A*, 515, A68
- Meurer, G. R., Heckman, T. M., Lehnert, M. D., et al. 1997, *AJ*, 114, 54
- Micheva, G., Iwata, I., Inoue, A. K., et al. 2017, *MNRAS*, 465, 316
- Mollá, M., García-Vargas, M. L., & Bressan, A. 2009, *MNRAS*, 398, 451
- Momose, R., Ouchi, M., Nakajima, K., et al. 2016, *MNRAS*, 457, 2318
- Nagao, T., Maiolino, R., & Marconi, A. 2006, *A&A*, 447, 863
- Nagao, T., Maiolino, R., Marconi, A., & Matsuhara, H. 2011, *A&A*, 526, 149
- Nakajima, K., Ouchi, M., Shimasaku, K., et al. 2013, *ApJ*, 769, 3
- Nakajima, K., & Ouchi, M. 2014, *MNRAS*, 442, 900
- Nakajima, K., Ellis, R. S., Iwata, I., et al. 2016, *ApJL*, 831, L9 (Paper I)
- Nakajima, K., Schaerer, D., Le Fèvre, O., et al. 2017, *A&A* in press, arXiv e-prints, arXiv:1709.03990
- Nestor, D. B., Shapley, A. E., Kornei, K. A., Steidel, C. C., & Siana, B. 2013, *ApJ*, 765, 47
- Nilsson, K. K., Tapken, C., G., Møller, P., et al. 2009, *A&A*, 498, 13
- Nilsson, K. K., Ostlin, G., Møller, P., et al. 2011, *A&A*, 529, A9
- Oesch, P. A., van Dokkum, P. G., Illingworth, G. D., et al. 2015, *ApJL*, 804, L30
- Ono, Y., Ouchi, M., Shimasaku, K., et al. 2010, *MNRAS*, 402, 1580
- Pérez-Montero, E., & Amorín, R. 2017, *MNRAS*, 467, 1287
- Reddy, N. A., Pettini, M., Steidel, C. C., et al. 2012, *ApJ*, 754, 25
- Reddy, N. A., Kriek, M., Shapley, A. E., et al. 2015, *ApJ*, 806, 259

**Table 5.** Properties of the VIMOS-LAEs with UV-line detection

Obj.	R.A.	Decl.	$M_{UV}$	EW(Ly $\alpha$ )	$z_{Ly\alpha}$	$\Delta v_{Ly\alpha}$	$\beta$	UV line(s)
	(1)	(1)	(2)	( $\text{\AA}$ ) (3)	(4)	( $\text{km s}^{-1}$ ) (5)	(6)	(7)
– NB497-selected –								
LAE86177	22:16:47.6	+00:17:51	$-19.3 \pm 0.2$	$111^{+33}_{-26}$	3.0734	–	$-2.32^{+0.68}_{-0.82}$	CIII], OIII] <sup>(†)</sup>
LAE104812	22:16:48.9	+00:21:41	$-20.3 \pm 0.1$	$23^{+6}_{-5}$	3.0967	–	–	CIII], OIII] <sup>(†)</sup> , HeII <sup>(†)</sup>
LAE82902	22:16:59.6	+00:17:16	$-20.1 \pm 0.1$	$120^{+15}_{-13}$	3.0717	–	$-1.50^{+0.34}_{-0.34}$	CIII], OIII] <sup>(†)</sup> , HeII <sup>(†)</sup>
LAE104037	22:17:06.7	+00:21:33	$-21.4 \pm 0.1$	$36^{+2}_{-2}$	3.0673	+194	$-1.62^{+0.08}_{-0.18}$	CIII], OIII], HeII
LAE94460	22:17:08.0	+00:19:32	$-19.9 \pm 0.1$	$51^{+8}_{-7}$	3.0744	+171	$-1.96^{+0.40}_{-0.36}$	CIII], OIII] <sup>(†)</sup>
LAE96549	22:17:26.3	+00:19:58	$-19.5 \pm 0.2$	$77^{+3}_{-3}$	3.0455	–	$-2.44^{+1.26}_{-1.50}$	CIII]
LAE84811	22:17:27.8	+00:17:37	$-19.0 \pm 0.3$	$270^{+101}_{-69}$	3.0928	–	$-1.20^{+1.04}_{-0.98}$	CIII]
LAE46348	22:17:30.4	+00:09:06	$-22.4 \pm 0.1$	$20^{+7}_{-7}$	3.1500	–	$-0.96^{+0.04}_{-0.04}$	CIII], CIV(+abs.)
LAE105870	22:17:33.3	+00:21:51	$-19.4 \pm 0.2$	$138^{+49}_{-35}$	3.0933	–	$-3.76^{+1.46}_{-0.24}$	CIII]
LAE52973	22:17:38.9	+00:11:02	$-21.0 \pm 0.1$	$81^{+7}_{-6}$	3.0654	–	$-1.42^{+0.10}_{-0.26}$	CIII], HeII <sup>(†)</sup>
LAE104357	22:17:42.6	+00:20:55	$-21.8 \pm 0.1$	$97^{+3}_{-3}$	3.1732	–	$-1.72^{+0.12}_{-0.10}$	CIII], CIV(+abs.), HeII
LAE65130	22:17:48.7	+00:13:33	$-20.2 \pm 0.1$	$412^{+64}_{-53}$	3.0565	–	$-1.34^{+0.36}_{-0.34}$	CIII]
LAE52126	22:17:56.4	+00:10:44	$-19.7 \pm 0.2$	$56^{+13}_{-11}$	3.1230	–	$-1.18^{+0.44}_{-0.54}$	CIII] <sup>(†)</sup> , OIII] <sup>(†)</sup>
AGN86861	22:17:09.6	+00:18:01	$-21.5 \pm 0.1$	$82^{+3}_{-2}$	3.1097	+338	$-2.38^{+0.08}_{-0.22}$	CIV, HeII, NV, HeII, CIII]
– UV-selected –								
LAE50416	22:17:08.1	+00:09:58	$-21.1 \pm 0.1$	$117^{+3}_{-3}$	3.2911	–	$-1.96^{+0.24}_{-0.28}$	CIII], OIII], CIV, HeII <sup>(†)</sup>

(1) Coordinates are in J2000. (2) Absolute UV magnitude. (3) Rest EW(Ly $\alpha$ ). For the NB497-selected LAEs, the EW is estimated from the BV–NB497 colour in conjunction with the Ly $\alpha$  redshift. The EW of UV-selected galaxy of LAE50416 is derived from spectroscopy. (4) Redshift determined with Ly $\alpha$ . (5) Velocity offset of Ly $\alpha$ . The systemic redshift is determined by the rest-frame optical emission lines provided by the MOSFIRE observation (Paper I). (6) UV continuum slope  $\beta$ . (7) UV emission line(s) except for Ly $\alpha$  identified with VIMOS. (†) Tentative detection.

Reddy, N. A., Oesch, P. A., Bouwens, R. J., et al. 2018, *ApJ*, 853, 56  
 Rigby, J. R., Bayliss, M. B., Gladders, M. D., et al. 2015, *ApJL*, 814, L6  
 Roberts-Borsani, G. W., Bouwens, R. J., Oesch, P. A., et al. 2016, *ApJ*, 823, 143  
 Robertson, B. E., Furlanetto, S. R., Schneider, E., et al. 2013, *ApJ*, 768, 71  
 Schaerer, D., Izotov, Y. I., Verhamme, A., Orlitová, I., Thuan, T. X., Worseck, G., & Guseva, N. G. 2016, *A&A*, 591, L8  
 Schenker, M. A., Ellis, R. S., Konidaris, N. P., & Stark, D. P. 2013, *ApJ*, 777, 67  
 Schlegel, D. J., Finkbeiner, D. P., & Davis, M. 1998, *ApJ*, 500, 525  
 Shapley, A. E., Steidel, C. C., Pettini, M., & Adelberger, K. L. 2003, *ApJ*, 588, 65  
 Shibuya, T., Ouchi, M., Nakajima, K., et al. 2014, *ApJ*, 788, 74  
 Shivaee, I., Reddy, N. A., Siana, B., et al. 2018, *ApJ*, 855, 42  
 Smit, R., Bouwens, R. J., Labbé, I., et al. 2014, *ApJ*, 784, 58  
 Smit, R., Bouwens, R. J., Franx, M., et al. 2015, *ApJ*, 801, 122  
 Song, M., Finkelstein, S. L., Gebhardt, K., et al. 2014, *ApJ*, 791, 3  
 Stanway, E. R., Eldridge, J. J. & Becker, G. D. 2015, *MNRAS*, 456, 485  
 Stark, D. P., Ellis, R. S., & Ouchi, M. 2011, *ApJ*, 728, L2  
 Stark, D. P., Richard, J., Siana, B., et al. 2014, *MNRAS*, 445, 3200  
 Stark, D. P., Richard, J., Charlot, S., et al. 2015a, *MNRAS*, 450, 1846  
 Stark, D. P., Walth, G., Charlot, S., et al. 2015b, *MNRAS*, 454, 1393  
 Stark, D. P., Ellis, R. S., Charlot, S., et al. 2017, *MNRAS*, 464, 469

Steidel, C. C., Strom, A. L., Pettini, M., Rudie, G. C., Reddy, N. A., & Trainor, R. 2016, *ApJ*, 826, 159  
 Trainor, R. F., Steidel, C. C., Strom, A. L., & Rudie, G. C. 2015, *ApJ*, 809, 89  
 Trainor, R. F., Strom, A. L., Steidel, C. C., & Rudie, G. C. 2016, *ApJ*, 832, 171  
 Vanzella, E., de Barros, S., Vasei, K., et al. 2016a, *ApJ*, 825, 41  
 Vanzella, E., de Barros, S., Cupani, G., et al. 2016b, *ApJ*, 821, 27  
 Verhamme, A., Orlitová, I., Schaerer, D., Izotov, Y. I., Worseck, G., Thuan, T. X., & Guseva, N. 2017, *A&A*, 597, A13  
 Villar-Martín, M., Tadhunter, C., & Clark, N. 1997, *A&A*, 323, 21  
 Wisotzki, L., Bacon, R., Blaizot, J., et al. 2016, *A&A*, 587, A98  
 Yamada, T., Nakamura, Y., Matsuda, Y., et al. 2012, *AJ*, 143, 79  
 Yang, H., Malhotra, S., Gronke, M., et al. 2017, *ApJ*, 844, 171  
 Zheng, Z & Wallace, J. 2014, *ApJ*, 794, 116